Journal of Fluids and Structures (1997) **11,** 717–744

THE NONLINEAR HYDROELASTIC BEHAVIOUR OF FLEXIBLE WALLS

A. D. Lucey, G. J. Cafolla, P. W. Carpenter and M. Yang
Department of Engineering, University of Warwick, Coventry, CV4 7AL, U.K.

(Received 7 January 1997 and in revised form 11 June 1997)

A computational model is developed to study the hydroelastic response of simple panels and compliant walls to a uniform flow. Numerical experiments are presented which simulate the history of hydroelastically unstable disturbances as they evolve from amplitudes that may be treated by linear theory to amplitudes for which non-linearity in both the wall and flow cannot be neglected. The method is first applied to simple unsupported flexible panels. Unstable deformations of these panels are seen to be dominated by the fundamental mode. When some panel damping is incorporated, the panel ultimately settles into a static buckled state; however, this long-time response may be preceded by sustained nonlinear oscillations. The amplitudes and frequencies of these oscillations are characterized as a function of wall and flow properties. The method is then used to study a compliant wall comprising a spring-backed flexible plate. For low levels of wall damping, linearly unstable waves evolve into a complex limit-cycle flutter-type response. For high levels of damping small-amplitude unstable disturbances evolve into saturated nonlinear divergence waves that have sharp peaks and shallow troughs. These have much slower downstream wave travel than small-amplitude growing divergence waves. Features of the simulated waves and their dependence on the freestream flow show good qualitative agreement with experimentally measured nonlinear divergence waves. The characteristic waveform of the nonlinear divergence waves is shown to be attributable to the hydrodynamic stiffness pressure field generated by large-amplitude disturbances.

1. INTRODUCTION

The interaction of a flexible panel with a fluid flow is a fundamental problem of aero- and hydroelasticity and one that has received attention for a number of decades. And yet this deceptively straightforward system – especially when uniform flow is assumed and a simple differential operator used to model the wall – continues to warrant further study. Predictions of the panel behaviour appear very sensitive to assumptions made in the system model. This is true even for the case of linearized theory where contradictory predictions can be obtained depending on whether an infinitely-long or a finite panel is modelled and whether or not structural damping is incorporated in the wall model. Moreover, the field of interest has expanded. In the nonlinear regime of response, features of dynamical systems may be manifest. The hydroelastic stability of flexible panels is also an essential ingredient in the design of drag-reducing compliant coatings. So too has interest recently grown in the area of active control of structure-borne sound when a mean flow is present. Review articles in these respective areas have been presented by Dowell (1975), Matsuzaki (1986), Riley *et al.* (1988), Carpenter (1990) and Crighton (1987).

In the present paper we apply the technique of numerical simulation to study the nonlinear behaviour of a finite flexible panel with pinned ends interacting with an incompressible uniform mean flow. To set the context for this work we first review some relevant

0889-9746/97/070717 + 28 $25.00/fl970107

linear studies which highlight the dependence of theoretical prediction upon the system model. Thereafter the discussion turns to experimental and existing nonlinear studies of the problem at hand.

Linear theoretical studies of the system by Dugundji *et al.* (1963), Weaver & Unny (1971), Ellen (1973), Garrad & Carpenter (1982b) and Lucey & Carpenter (1993b) all predict that the panel first loses its stability to static divergence. For a simple unsupported panel the critical mode is the fundamental. When a further restorative structural component is present – for example a uniform spring foundation – a most dangerous mode can be identified as having the lowest critical flow speed for instability onset; the wavelength of this mode is a function of a combination of wall properties. At flow speeds lower than the critical flow speed, neutrally stable waves (in the absence of structural damping) characterize the panel response to disturbances. Single-mode static divergence is predicted to dominate for a range of flow speeds beyond the critical value, until further increases see this instability stabilizing before giving way to a more severe modal-coalescence flutter instability. This flutter appears as a downstream travelling, amplifying wave. A similar transition with a rise in flow speed – from neutral stability to divergence to flutter instability – is found in equivalent studies of infinitely long panels [for example see Benjamin (1963), Djugundi *et al.* (1963), Kornecki (1978)]. Carpenter & Garrad (1986) showed exact equivalence between predictions for long finite and infinite panels regarding the divergence-onset flow speed and the wavelength of the most dangerous mode. However, in studies of an infinite panel it has been necessary to model the structural damping of the panel in order to realize divergence. Furthermore, at flow speeds in excess of the critical value, the divergence instability is predicted to be a slow, downstream-travelling, amplifying wave in contrast to the static instability predicted by the studies of a finite panel.

The numerical simulations of Lucey & Carpenter (1992a, b) for the linear problem of a finite panel showed agreement with the theoretical divergence-onset flow-speed predictions discussed in the preceding paragraph. However, the numerical simulations showed that divergence instability takes the form of a downstream-travelling wave and that damping plays only a conventional role in the flow-structure system in that it reduces the rate of wave amplification. It would therefore seem that the theoretical studies of finite panels overconstrain the problem when prescribing a disturbance form represented by a finite number of orthogonal modes. Whilst predicting a travelling form of instability, the theoretical studies of an infinite panel wrongly characterize the effect of structural damping. For very long, but finite, panels, Lucey & Carpenter (1993a) have suggested that fixed panel ends play a role equivalent to that required of structural damping in the realization of divergence when a panel of infinite length is modelled. Moreover, the numerical simulations showed that there was no clear boundary between divergence instability and modal-coalescence flutter. This was in marked contrast to theoretical studies of finite panels which predict the onset of flutter to be a distinct and explosive phenomenon.

Experimental studies of simple unsupported panels, for example Gislason (1971), show that the panel buckles in the fundamental mode. The experiments of Dugundji *et al.* (1963) which used a spring-backed panel, for which the most dangerous mode is not the fundamental, did not convincingly show static divergence. However, they clearly did measure a flutter-type instability which could be associated with the modal-coalescence flutter predicted by linear theory. Moreover this flutter-type behaviour persisted into the nonlinear regime of disturbance amplitude. Detailed experiments on divergence conducted by Gad-el-Hak *et al.* (1984) find the instability to take the form of a slow downstream-travelling wave. For the range of flow speeds used in the experiments, divergence was only

found when the boundary layer was turbulent rather than laminar. The flexible boundary in this case was a homogeneous viscoelastic layer with high internal damping. Gad-el-Hak's (1986) experiments on an elastic wall (with low damping) did not yield divergence. Instead, a different instability – travelling-wave flutter – was identified; the mechanism for this instability is one of irreversible energy transfer to the wall by the action of the boundary layer. These differences led Gad-el-Hak *et al.* (1984) to infer that the action of wall damping was crucial in the mechanism which causes divergence instability. However, Lucey & Carpenter (1992a) have suggested that the viscoelastic wall damping only served to facilitate the formation of the most dangerous mode when a continuous source of excitation was present due to the turbulent boundary layer. It was particulary noteworthy that the nonlinear surface deformations due to divergence instability on the strongly damped wall of Gad-el-Hak *et al.* (1984) differed greatly from the mainly sinusoidal profiles found in experiments on lightly damped flexible surfaces (Dugundji *et al.* 1963; Gad-el-Hak 1986). When divergence instability developed in the linear numerical simulations of Lucey & Carpenter (1992a, b) it took a broadly sinusoidal profile, thereby justifying the disturbance forms assumed in theoretical studies of both finite and infinite flexible walls. In contrast, Gad-el-Hak *et al.* (1984) described typical nonlinear divergence profiles as comprising sharp peaks separated by wide shallow valleys. Thus in nonlinear theoretical studies, an over-constrained presupposition of instability form could lead to erroneous predictions. In the present paper, this obstacle to theoretical modelling is overcome by the use of numerical simulation, because the flexible panel is allowed to develop into a nonlinear disturbance profile which may be different from a profile which is unstable to small disturbances.

Previously, theoretical modelling of the interaction between a uniform flow and nonlinear disturbances of a flexible panel has largely followed the technique used for linear studies. The wall profile has been assumed to take the form $\exp(\mathrm{i}\omega t)\sum_{n=1}^{N} A_n f_n(x)$ where ω is the radian frequency of the disturbance and $f_n(x)$ represent a set of spatially orthogonal functions satisfying the leading- and trailing-edge boundary conditions, with A_n being the (complex) amplitudes of these modes. Ellen (1977) used just a fundamental sinusoidal mode in his study of an unsupported panel. This simplification allowed nonlinear effects in both the wall and the perturbed flow field to be modelled. The destabilizing fluid forces in the linear regime were found to be overcome by the restorative structural forces as the deformation grew. In the absence of structural damping, limit-cycle behaviour about a buckled configuration was predicted; when structural damping was incorporated, the panel settled into the static buckled state. Matsuzaki (1981) studied the stability of a spring-backed panel using one-, two- and three-mode expansions of the panel deformation. The combination of modes used were such that incompressibility of the flow was not violated. Nonlinear panel dynamics were modelled, but generalized hydrodynamic forces derived for linear disturbances in Matsuzaki & Ueda (1980) were used for the fluid forcing. The analysis investigated the behaviour of disturbances about the buckled configurations predicted by linear theory. With panel damping present, limit-cycle behaviour was not predicted and the panel settled into a non-trivial static configuration dominated by the single mode which was most unstable at small amplitudes. The identity of this mode depended on the applied flow speed. This was also the principal finding in the subsonic section of Reynolds & Dowell's (1993) investigation. Again, a linear flow solution was applied to a nonlinear equation for a damped spring-backed panel and perturbations about flat and buckled (statically diverged) states were investigated. However, in arriving at their conclusions, Reynolds & Dowell (1993) included up to twelve modes in the expansion for the disturbance profile.

The consensus of nonlinear theoretical models of a damped wall-flow system indicates that fluttering panel motions ultimately give way to a stable buckled configuration as the disturbance amplitude increases. Matsuzaki (1986) therefore finds an equivalence between this prediction and the analysis of Holmes (1978), which showed that flexible pipes supported at both ends cannot flutter. However, Holmes recognizes that flexible pipes do flutter in reality. This then challenges the assumptions used in existing theoretical models of the present system. It has been noted above that, even in the linear regime, the use of a modal expansion *a priori* yields a strictly static divergence as the first instability encountered with a rise in flow speed, whereas in reality divergence manifests itself as a slowly travelling wave. Thus, nonlinear analyses based upon perturbations about a static deformation can be called into question. It would also appear from experimental results that the level of damping in the flexible wall has a strong influence upon the deformations found at flow speeds above the critical value.

The present paper accordingly attempts to resolve uncertainties attributable to the limitations in existing theoretical approaches. We model nonlinear effects in both the wall and fluid dynamics for a flexible panel/wall. Firstly we investigate the response of a simple plate held at both its ends. We show that, provided damping is present, the plate comes to rest in a static buckled state as time tends to infinity. For finite times, we characterize the amplitudes and frequencies of the nonlinear oscillations that may persist for quite some time when the levels of damping are those associated with realistic metal panels. We then turn our attention to the response of a compliant panel modelled as a spring-backed flexible plate for which the critical mode is of higher order than the fundamental. In doing so we find that for very lightly damped panels a form of travelling-wave limit-cycle behaviour persists. We present only limited results for such panels. In contrast, heavily damped panels settle into a nearly static deformation. For these the nonlinear waveform is very different – in both shape and phase speed – from the linearly unstable mode from which it develops.

The layout of the paper is as follows. In Section 2 we outline the numerical methods used in the coupled wall-flow solution. Results of typical numerical experiments are presented in Section 3; here we investigate the use of a linear flow solution with a nonlinear wall in addition to presenting results obtained by modelling non-linear effects in both wall and fluid. Finally, in Section 4, the main findings of the present study are summarized.

2. METHOD

2.1. Formulation

The equation of motion [e.g. see Dowell (1975)] for vertical displacements, $w(x, t)$ of the spring-backed flexible panel illustrated in Figure 1(a) is

$$\rho_W h\ddot{w} + d\dot{w} - T_I(w_{,x})w_{,xx} + Bw_{,xxxx} + Kw = -\Delta p(\ddot{w}, \dot{w}, w), \tag{1}$$

where ρ_W, h, d are, respectively, the density, thickness and damping coefficient of the panel, whilst K is the coefficient of the spring-foundation stiffness. Here, the dot and suffix notation respectively indicate temporal and spatial differentiation. On the right-hand side, the action of the fluid flow is represented by the nonlinear perturbation pressure, Δp. The flexural rigidity of the plate, B, and the induced tension, T_I, are given by

$$B = \frac{Eh^3}{12(1-\nu^2)}, \quad T_I = \frac{Eh}{L(1-\nu^2)} \int_0^L [(1 - w_{,x}^2)^{1/2} - 1]\,\mathrm{d}x, \tag{2a, b}$$

where E, v and L are, respectively, the elastic modulus, Poisson ratio and undeformed length of the flexible plate. This simplified nonlinear model of the wall mechanics follows that of Matsuzaki (1981) and Reynolds & Dowell (1993).

To evaluate the fluid perturbation pressure, we assume unsteady potential flow. In reality, the presence of a viscous boundary layer would mean that the fluid pressure at the wall would differ from that generated by disturbances to the potential flow beyond the boundary layer. However, for the types of hydroelastic phenomena investigated here, the effect of the boundary layer can be modelled [for example, Duncan *et al.* (1985)] by scaling the potential-flow perturbation pressure using a factor of the form $K_p \exp(\mathrm{i}\psi)$. This strategy is based upon experimental work by Kendall (1970) for turbulent boundary layers and numerical work by Balasubramanian & Orszag (1983) for laminar boundary layers who identified approximate values for K_p and ψ; these are dependent upon surface-wave characteristics and boundary-layer thickness. In the present context, K_p is the most significant. For the unsupported plate studied in Section 3.1 it would be very close to unity, but for the low-wavelength disturbances of Section 3.2 it would be substantially less than unity. Moreover, in the latter case, the laminar K_p value would be typically 25% of the equivalent turbulent-boundary-layer value. In the present work we do not use such a scaling factor because it is a complex function of wave-disturbance characteristics. Thus we assume that $K_p = 1$ and $\psi = 0$, but recognize that the present model overestimates the magnitude of the destabilizing fluid forces, and that our results for the compliant panel will be more appropriate to turbulent rather than laminar boundary-layers.

The flow field is written as

$$\mathbf{u}(\mathbf{x}, t) = U_\infty \mathbf{i} + \nabla\phi(\mathbf{x}, t), \tag{3}$$

where $\mathbf{x} = (x, y)$ and ϕ is a perturbation potential satisfying the Laplace equation. The perturbation potential is generated by integrating a distribution of sources of intensity σ over the wall-flow interface, $\mathbf{x}_s$, thereby giving:

$$\phi(\mathbf{x}, t) = \frac{1}{2\pi} \int \sigma(\mathbf{x}_s, \mathbf{t}) \ln |\mathbf{x} - \mathbf{x}_s(t)| \, \mathrm{d}s. \tag{4}$$

The source strengths are evaluated by imposing the no-flux boundary condition,

$$(U_\infty \mathbf{i} + \nabla\phi(\mathbf{x}, t)) \cdot \mathbf{n} = U_N \tag{5}$$

on the surface of the flexible panel and adjacent rigid wall. Here $\mathbf{n}$ and U_N are, respectively, the unit vector and wall speed in the direction of the outward normal of the wall-flow interface. Having evaluated the perturbation potential, the unsteady Bernoulli equation can be used along the interfacial surface streamline to evaluate the perturbation pressure which drives the wall motion.

2.2. Flow Solution

The flexible-panel/flow interface is discretized into a set of M boundary elements (or panels), as suggested by Figure 1. The source strengths in equation (4) are assumed constant over each boundary element. Thus, from standard panel-method techniques [see Hess & Smith (1966)], the disturbance normal velocity, velocity potential and tangential velocity

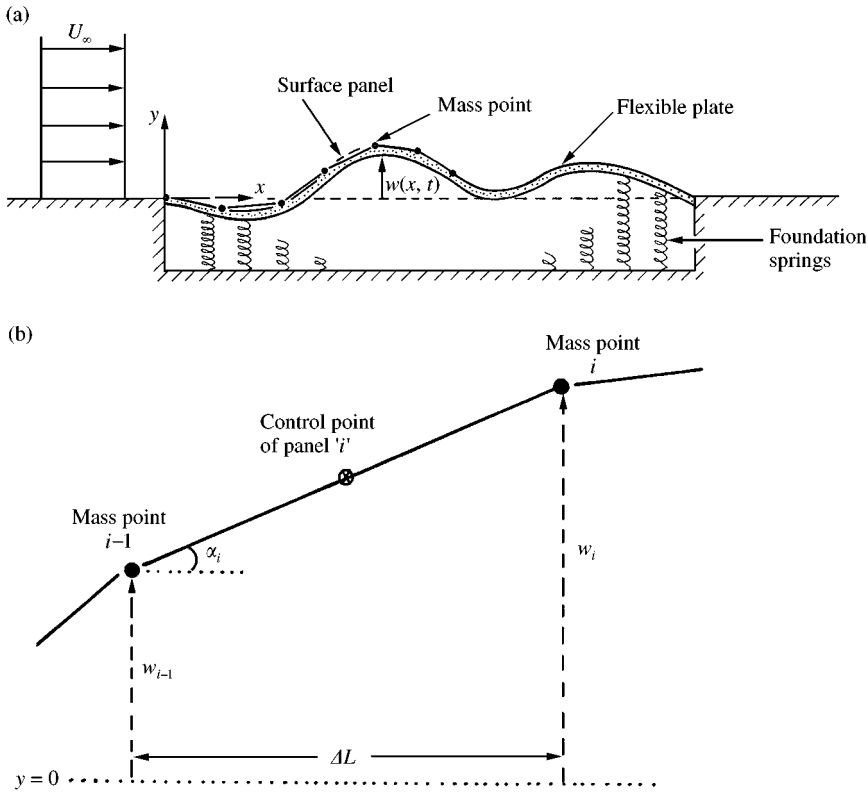

Figure 1. (a) Schematic of the flexible panel in a uniform flow; (b) detail giving boundary-element notation.

induced at each panel, $\mathbf{i}$: $0 \rightarrow M$, are respectively given by

$$u_{Ni} = N_{im}\sigma_m, \tag{6a}$$

$$\phi_i = \Phi_{im}\sigma_m, \tag{6b}$$

$$u_{Ti} = T^{\sigma}_{im}\sigma_m + T^{\lambda}_{im}\lambda_m, \tag{6c}$$

where repeated suffices imply summation. The matrices N_{im}, Φ_{im}, T^{σ}_{im} and T^{λ}_{im} are influence coefficients which depend solely upon the geometry of the interface; expressions for these are given in the appendix. The evaluations are carried out at control points, chosen here to be at panel mid-points. In evaluating the tangential velocities, the source strength has been 'smeared' over the panel as a linear variation with coefficient λ_i given by a forward-difference gradient of sources strengths on adjacent panels. This strategy was used by Lucey & Carpenter (1992a) to improve the accuracy of the hydrodynamic-stiffness term in the pressure without recourse to excessively fine discretizations. This approximates a second-order panel method (Hess 1973) for the hydrodynamic stiffness, whilst evaluations of hydrodynamic damping and inertia remain at first order.

For nonlinear disturbances the deforming surface and rigid surround should be discretized in the boundary-element method with zero normal velocity imposed on both flexible and rigid wall-flow interfaces. In contrast to a linearized flow solution, this is

because the nonlinear perturbation potential associated with deformations to the panel can induce non-zero normal velocity component on the rigid surround. However, our investigations using a fully meshed wall-flow interface have shown that the rigid surround exercises negligible hydrodynamic effect on the flexible boundary. This is especially so for modes of higher order and thus the discretizations used herein only map a set of panels over the deforming surface. The discretization is such that all panels have length $\Delta L = L/M$ when projected onto the plane $y = 0$. The notation adopted for a panel and the lumped-mass points at its ends is shown in Figure 1(b). The discretized form of the boundary condition, equation (5), is used to write the following matrix equation which determines the required panel source strengths:

$$N_{im}\sigma_m = U_\infty \sin\alpha_i + U_{Ni}, \tag{7}$$

where $\sin\alpha_i$ is the slope of panel i and the m-summation is over the M surface panels.

2.3. Pressure Evaluation

The unsteady perturbation pressure is evaluated at each boundary-element control point using the Bernoulli equation:

$$\Delta p_i = \underbrace{\tfrac{1}{2}\rho(U_\infty^2 - (U_\infty \cos\alpha_i + u_{Ti})^2 - U_{Ni}^2)}_{\text{(i)}} - \underbrace{\rho\dot{\phi}_i}_{\text{(ii)}}, \tag{8}$$

where ρ is the fluid density. The hydrodynamic stiffness and part of the damping are represented by term (i) which is evaluated using equation (6c). We note that this term is $\mathcal{O}(w)$ with nonlinear effects entering at $\mathcal{O}(w^2)$. However, it will be seen in Section 3.1 that, for an unsupported panel, the $\mathcal{O}(w^3)$ nonlinear structural effects are more important than those of the flow. Term (ii) yields the rest of the damping and all of the hydrodynamic inertia. To evaluate term (ii), we note from equation (6b) that

$$\dot{\phi}_i = \Phi_{im}\dot{\sigma}_m + \dot{\Phi}_{im}\sigma_m. \tag{9}$$

The second term is higher order than the first and is approximated using a backward-difference time-step for $\dot{\Phi}_{im}(\dot{w}, w)$. For the first term, an expression for $\dot{\sigma}_i$ is found from equation (7):

$$\dot{\sigma}_i = N_{im}^{-1}(U_\infty \dot{\alpha}_i \cos\alpha_i + \dot{U}_{Ni}) - N_{in}^{-1}\dot{N}_{nm}\sigma_m. \tag{10}$$

Again, the second term is of higher order and so $\dot{N}_{nm}(\dot{w}, w)$ is also approximated using a backward-difference time step. It will be seen in equation (11) below that neither of the terms in equations (9) and (10) which have required numerical approximation are functions of wall acceleration. From the definition of α_i in Figure 1(b) and noting that $U_{Ni} = \{(\dot{w}_{i+1} + \dot{w}_i)\cos\alpha_i\}/2$, equation (10) is used in equation (9) to give

$$\begin{aligned}\dot{\phi}_i = {} & \Phi_{im}N_{mn}^{-1}[\{\cos(\alpha)/2\}_n \times (\{\ddot{w}\}_n + \{\ddot{w}\}_{n-1})] + \Phi_{im}N_{mn}^{-1}\{U_\infty \dot{\alpha}\cos(\alpha)\}_n \\ & - \Phi_{im}N_{mn}^{-1}[\{\dot{\alpha}\sin(\alpha)/2\}_n \times (\{\dot{w}\}_n + \{\dot{w}\}_{n-1})] + [\dot{\Phi}_{in} - \Phi_{im}N_{mj}^{-1}\dot{N}_{jn}]\sigma_n,\end{aligned} \tag{11}$$

where the $\times$-notation means an element by element multiplication of the two vectors in braces. After multiplying equation (11) by ρ, the first, $\ddot{w}_i$-dependent, term gives an explicit expression for the hydrodynamic inertia. Isolating the hydrodynamic-inertia term allows it to be combined with the structural inertia in the coupled wall-flow solution procedure detailed in Section 2.4 below. In wall-flow structure interactions where the fluid inertia

greatly exceeds the wall inertia, the lumping of inertias is essential for numerical stability of the coupled system when solving for the wall-acceleration in the presence of fluid loading. This was the strategy adopted in the equivalent linear problem of Lucey & Carpenter (1992a) and has found application in the more complex fluid-loading problem studied by Davies & Carpenter (1997).

2.4. Numerical Scheme for Coupled Wall-flow Solution

The wall equation is written in finite-difference form and solved using an implicit time-marching scheme with increment δt. The two time-differencing equations followed by the wall equation are written in the form:

$$w_i^{t+\delta t} = w_i^t + \delta t(\dot{w}_i^t + \dot{w}_i^{t+\delta t})/2, \tag{12a}$$

$$\dot{w}_i^{t+\delta t} = \dot{w}_i^t + \delta t(\ddot{w}_i^t + \ddot{w}_i^{t+\delta t})/2, \tag{12b}$$

$$B_{im}\ddot{w}_m^{t+\delta t} = F_i(\dot{w}^{t+\delta t}, w^{t+\delta t}), \tag{12c}$$

where B_{im} represents the inertias of both wall and fluid. The latter obtain from the first two terms on the right-hand side of equation (11) and averaging the contribution of adjacent panels straddling the mass point. Thus the wall-flow inertia matrix is

$$B_{im} = \rho_W h\delta_{im} - \rho(I_{im} + I_{i+1,m} + I_{i,m+1} + I_{i+1,m+1}), \tag{13}$$

where I_{im} is a matrix assembled by multiplying each element m of row i in the matrix $\Phi_{in}N_{nm}^{-1}$ by $\cos\alpha_m^{t+\delta t}/4$.

The forcing term F_i in the right-hand side of equation (12c) is assembled using the remaining terms of the perturbation pressure together with the wall damping and stiffness terms. Again, adjacent control-point pressures are averaged to yield the mass-point pressure term, $\Delta\bar{p}$. These pressure terms combine the first term on the right-hand side of equation (8) and the last three terms of equation (11). Thus,

$$F_i = -\Delta\bar{p}(\dot{w}^{t+\delta t}, w^{t+\delta t}) - d\dot{w}_i^{t+\delta t} - Bw_{,xxxx}^{t+\delta t}|_i - K_E w_i^{t+\delta t} + \frac{Eh}{(1-\nu^2)}\sum_{j=1}^{M}\frac{[(1-\tan^2\alpha_j^{t+\delta t})^{1/2}-1]}{M}w_{,xx}^{t+\delta t}|_i, \tag{14}$$

where $w_{,xx}|_i$ and $w_{,xxxx}|_i$ are found using centred differences.

Equations (12a, b, c) are solved using repeated sweeps through the array of mass-points updating each of $\ddot{w}^{t+\delta t}, \dot{w}^{t+\delta t}$ and $w^{t+\delta t}$ until all of these converge. Results from the fully implicit scheme described above have been compared with those of a semi-implicit scheme, wherein the pressure terms, $\bar{p}$, are evaluated only at the start of the time step. Whilst yielding accurate results in the linear regime of disturbances, the semi-implicit scheme generates numerical dissipation for nonlinear oscillations. The level of dissipation is reduced when the time-step is decreased. Thus the apparent computational savings available to the semi-implicit scheme are effectively cancelled by the finer temporal discretizations required if accurate results are to be obtained. Thus, in the following results pertaining to an unsupported panel in Section 3.1, a fully implicit scheme has been used. However, for the investigation of a highly damped compliant panel in Section 3.2 we have found it sufficient to use a semi-implicit scheme [following Lucey & Carpenter (1992a)]. This is because the non-linear divergence waves which evolve are nearly static; for these simulations, checks against equivalent results obtained using the fully implicit scheme have been conducted.

2.5. Linearization of the Flow Solution

In the results that follow, we discuss the results of some numerical experiments for which the nonlinear wall mechanics interact with a linear flow solution. For such cases, the formulation of Section 2.3 above is adapted as follows. The pressure evaluation, equation (8), linearized for small disturbances takes the form

$$\Delta p_i = \rho U_\infty u_{Ti} - \rho \dot{\phi}_i, \tag{15}$$

where $\dot{\phi}_i$ is found from the modified form of equation (11), which becomes

$$\dot{\phi}_i = \Phi_{im}(\ddot{w}_m + \ddot{w}_{m-1}) + \Phi_{im} 2U_\infty \dot{\alpha}_m, \tag{16}$$

having used $N_{im} = \delta_{im}/2$. Linearized forms for all of the influence coefficients used in equations (6) are included in the appendix. Note that the linearized influence coefficients need only be calculated once – at the start of a simulation – because they are independent of the wall deflection. Thereafter the solution procedure is identical to that presented in Section 2.4, except that the matrix I_{im} is replaced by Φ_{im} in equation (13).

3. RESULTS AND DISCUSSION OF NUMERICAL EXPERIMENTS

The results presented here have principally been obtained from the full non-linear computational model of the wall-flow system. However, we also conduct some numerical experiments with a linearized flow solution interacting with nonlinear wall mechanics. Together with the full results, this simplification allows us to determine separately the importance of nonlinearity in the wall and flow models. Furthermore, results of the simpler system can be compared against the analytical predictions of Matsuzaki (1981) and Reynolds & Dowell (1993) where a linearized flow solution was used. The results that follow are divided into two classes of aero/hydro-elastic investigation. The first concerns a flexible plate held at both its ends for which the critical mode is the fundamental. The second class is a flexible plate with a spring foundation in which the additional structural component raises the order of the critical mode. In the second type of problem, the panel edges play only a minor role in the determination of stability bounds and the results generated therein may be considered applicable to flexible or compliant walls of infinite extent.

3.1. Flexible Plate

In the absence of a spring foundation, the critical flow speed with respect to the growth of small disturbances occurs for the fundamental mode of deformation with wavelength $L/2$. A nondimensional stiffness ratio (destabilizing hydrodynamic stiffness to restorative wall forces), Λ^F, is introduced, where

$$\Lambda^F = \frac{\rho U_\infty^2 L^3}{B} = \frac{12\rho U_\infty^2}{E^*}(h/L)^{-3}, \tag{17}$$

in which $E^* = E/(1 - \nu^2)$. The key geometric parameter is therefore h/L. With hinged leading and trailing edges, divergence instability occurs for Λ^F greater than a critical value, Λ_D^F of about 40·1 [see the linear analyses of, for example, Ishii (1965), Weaver & Unny (1971), Ellen (1973), Garrad & Carpenter (1982b)]. Ellen (1977) conducted a nonlinear steady-state analysis based, again, on the fundamental mode of deformation and showed that the structural nonlinearity increases the critical value of Λ^F, whilst hydrodynamic

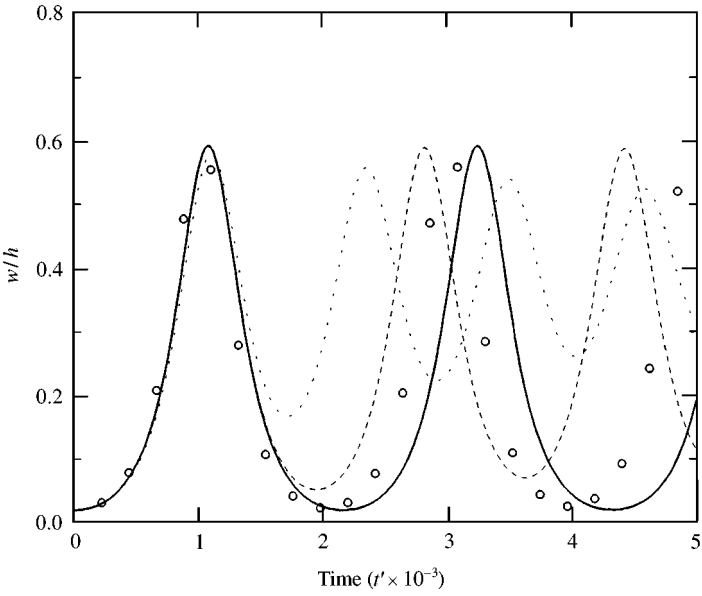

Figure 2. Deflection history of panel mid-point for $\Lambda^F = 61$. Continuous data is for nonlinear flow solution: ——, no wall damping; – –, 5% wall damping; - - - , 50% wall damping. Discrete data (○) is for linear flow solution with no wall damping.

nonlinearity marginally reduces its value. For realistic panels, Ellen shows that the structural nonlinearity far outweighs its hydrodynamic counterpart. This finding is reproduced in the present dynamic study of the simple panel. It is emphasized, however, that the present methods allow a natural development of the deformation, including the possibility of wave travel, a feature precluded in single-mode analyses. This then permits the change, with further rise in Λ^F beyond its critical value, from a buckling type of instability – associated with divergence – to a flutter-type of instability formed by the coalescence of the fundamental and the second mode.

Figures 2–5 show results for a stiffness ratio, $\Lambda^F = 61$, which is above the critical value found in linear studies. The value of h/L is 0·01 for these figures and a density ratio, ρ_W/ρ, of 2·6 has been used throughout this section. In Figures 2–5 such values could represent data for an aluminium panel of length 1 m and thickness 1 cm responding to a water flow of 20 m/s. To initiate the response characterized by Figures 2 and 3, the panel is released from a small-amplitude (of magnitudes $h/50$) deformation in the form of the fundamental mode. Figure 2† plots the time-history of the panel mid-point using nondimensional deflection and time defined by

$$w' = w/h, \qquad t' = \frac{\sqrt{E^*/\rho_W}}{L}\, t. \tag{18a,b}$$

† In generating Figure 2, $M = 10$ has been determined to be a suitable mesh size; for 1 cycle ($t' : 0 \rightarrow 2{\cdot}2 \times 10^3$) of the undamped wall, 2000 time-steps were needed. Each time-step required approximately five iterations of equations (12a–c) and took 1 second of CPU time on SUN SPARC Ultra 170E running at 167 MHz.

At small amplitudes, there is exponential growth of the disturbance which is predicted by linear studies. Using the data of Figure 2, the growth rate can be determined for the linear phase of response after the start-up process. If the temporal behaviour is assumed to be proportional to $\exp(-i\omega' t')$ (where the non-dimensional complex frequency is $\omega' = \omega'_R + \omega'_I i$), then the numerical experiment gives $\omega'_I = 4{\cdot}24 \times 10^{-3}$. This compares with a value of $4{\cdot}76 \times 10^{-3}$ predicted by a single-mode linear analysis using the methods of Garrad & Carpenter (1982b). The similarity of these figures confirms, to some extent, the integrity of the present numerical method. Exact agreement could not be expected because, in the present work, nonlinear effects in both flow and wall would be expected to reduce the growth rate marginally even at these amplitudes. In the results of Figure 2, note that the linear-flow solution generates slightly more rapid amplification than its nonlinear equivalent.

The initial dynamic growth seen in Figure 2 is then halted by the induced tension in the plate and nonlinear oscillations ensue. The results for a damped panel, also presented in Figure 2, (where n% damping means that the amplitude of linear oscillations *in vacuo* is reduced by a factor of $(1 - n)/100$ for each cycle) show these oscillations to be attenuated until a steady buckled state is reached. Nevertheless, it is remarked that for a lightly damped two-dimensional panel, large-amplitude oscillations could persist for many cycles. In Figure 2, the equivalent results found by using a linear flow solution show that whilst the peak deflection continues to be accurately predicted, the frequency of the ensuing large-amplitude oscillations is poorly represented. The evolution of the undamped panel deformation is shown in Figure 3(a, b) which cover one cycle. It is noted that early in the amplifying phase [Figure 3(a)] the point of maximum amplitude at successive times moves in the downstream direction; this feature was found in the simulations of unstable divergence waves by Lucey & Carpenter (1992a). It also provides a further reason why the growth rate, ω_I, found in the linear phase of the present numerical simulations should be lower than that determined by linear theory in which divergence instability is predicted to take the form of a single standing-wave mode. Beyond the mean amplitude of the cycle, during which inertial as opposed to hydrodynamic-stiffness effects cause the continued growth, the point of maximum amplitude at each time-step moves in the upstream

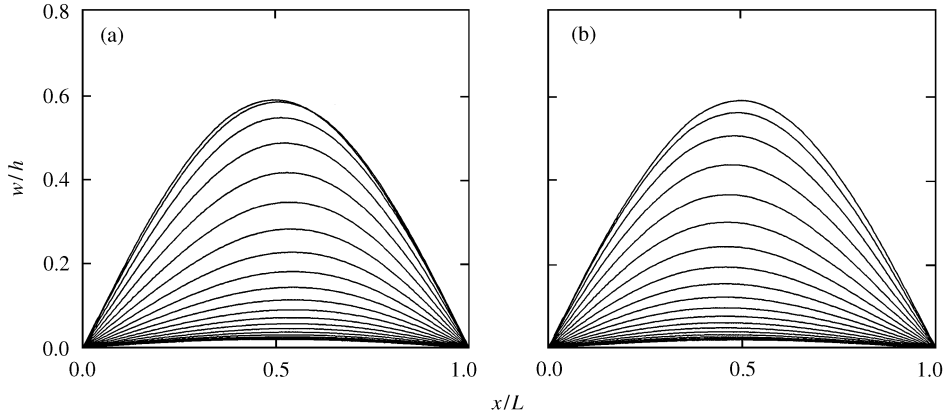

Figure 3. Instantaneous panel profiles at successive time-steps (increment $\delta t' = 0{\cdot}055 \times 10^3$) over one cycle of oscillation at $\Lambda^F = 61$ and zero wall damping; small-amplitude (of magnitude $h/50$) initial deflection: (a) amplifying phase; (b) attenuating phase.

direction. This sequence of events is exactly reversed in the attenuating phase of the cycle shown in Figure 3(b). This is borne out by the phase portrait presented in Figure 4. The innermost orbits around the attractors marked on the horizontal axis represent the (undamped) motion of the mid-point tracked in Figure 2. The larger deformed orbits centred on the origin illustrate the motion of the mid-point when the panel motion is initiated by a fundamental-mode deformation with an amplitude greater than the peak value attained by instability growth as seen in Figures 2 and 3. A typical cycle of oscillation for an initial amplitude equal to h is presented in Figure 5; this corresponds to the outermost orbit of Figure 4. The oscillations are characterized by the fundamental mode at the extremes of amplitude. However, it can be seen that, as the panel nears the zero-deflection axis, the deformation takes the shape of the next harmonic, thereby distributing the overall energy between kinetic and strain forms. It is remarked that the phase portrait of Figure 4 agrees well with that postulated by Ellen (1977), although we find reflectional symmetry about the zero-displacement axis. This is not inherent in the form of the dynamical equation suggested by Ellen for the wall-flow system. As predicted by Ellen, we find that the inclusion of plate damping causes the mid-point path to spiral in towards one of the attractors of Figure 4 regardless of the amplitude of initiation. This is precisely the way in which the attractors have been located in the present work.

For higher values of the stiffness ratio, Λ^F, surface wave-travel is promoted in the amplifying linear phase of response. Figure 6 shows the surface response of an undamped panel at $\Lambda^F = 244$ over one cycle of oscillation and is analogous to Figure 3. This value of Λ^F is below that at which modal-coalescence flutter of the first two modes is predicted by the linear studies of Weaver & Unny (1971) and Garrad & Carpenter (1982b). As suggested by Lucey & Carpenter (1992a), there is no clear distinction between divergence and modal-coalescence flutter when a less-constrained system model is used. At high

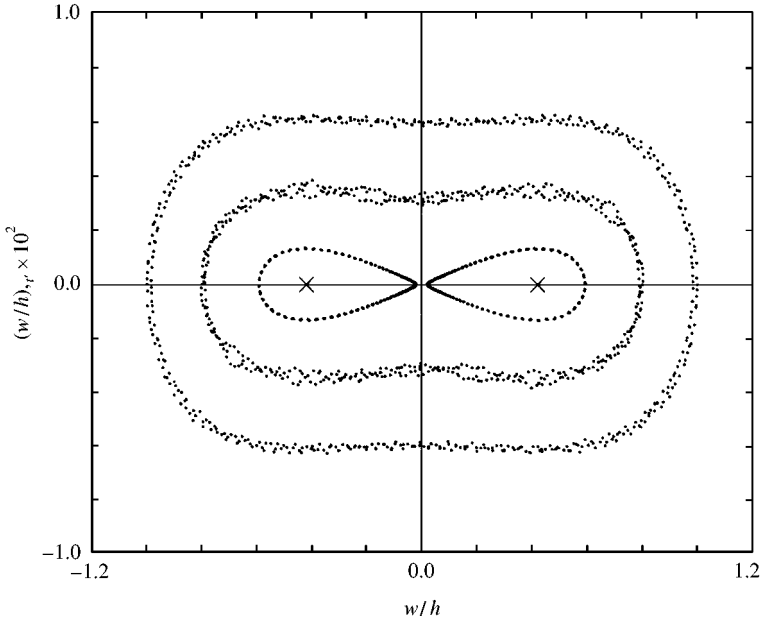

Figure 4. Phase portrait for undamped panel mid-point responses at $\Lambda^F = 61.$ × denotes locations at attractors.

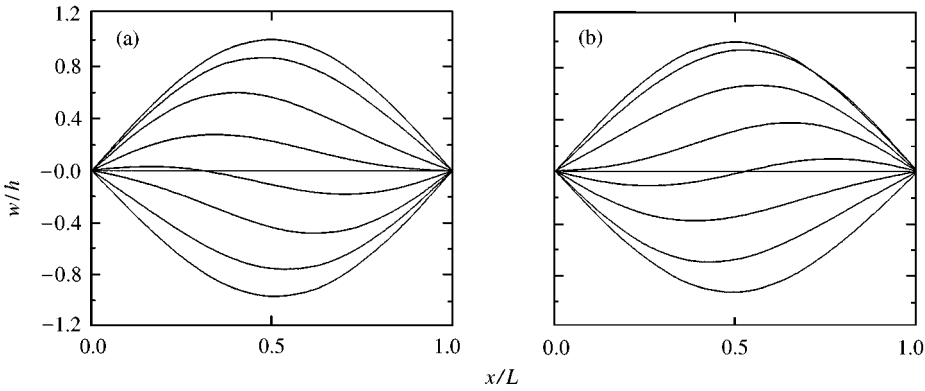

Figure 5. Instantaneous panel profiles at successive time-steps (increment $\delta t' = 0{\cdot}055 \times 10^3$) after a large, *positive*-amplitude (of magnitude h) initial deflection; all other parameters are identical to those of Figure 3(a) First half of one cycle; (b) second half of one cycle.

amplitudes, the fundamental mode favoured by the structural nonlinearity is seen to be dominant.

The illustrative results already presented indicate that for $\Lambda^F > \Lambda_D^F$ the growth of small disturbances is curtailed by the nonlinearity of the wall mechanics and thereafter nonlinear oscillations ensue. In physical applications, this seems the most likely course of events as opposed to the external imposition of a large-amplitude initiating deformation. Further numerical experiments have been conducted to establish the dependence on both Λ^F and the geometric parameter of the system, h/L, of both the maximum amplitude attained and the nonlinear oscillation frequency that characterize the response of a lightly damped flexible panel.

The discrete data in Figure 7 show the variation of the nondimensional maximum deformation magnitude, A/h, of an undamped oscillating panel with stiffness ratio, Λ^F, for different panel thickness/length ratios. The data plotted are obtained by releasing the panel

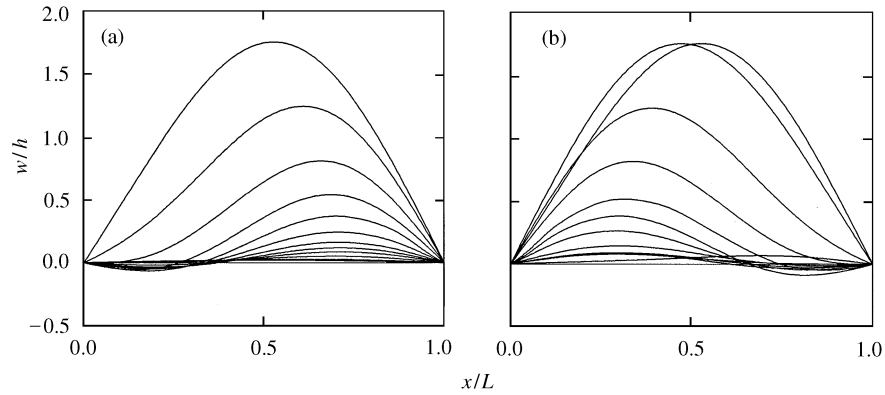

Figure 6. Instantaneous panel profiles at successive time-steps (increment $\delta t' = 0{\cdot}055 \times 10^3$) over one cycle of oscillation at $\Lambda^F = 244$; all other parameters and initial deflection are identical to those of Figure 3. (a) Amplifying phase; (b) attenuating phase.

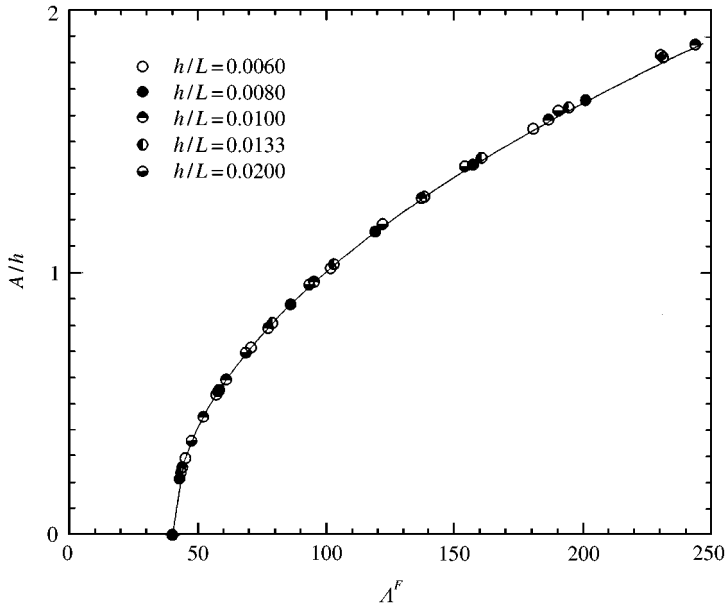

Figure 7. Variation of nondimensional maximum panel amplitude with stiffness ratio, $\Lambda^F(=\rho U_\infty^2 L^3/B)$, for different values of the geometric parameter, h/L. Data for the best-fit line are generated by equation (19).

from a very small amplitude (of magnitude $h/50$) initial static perturbation in the form of the fundamental sinusoidal mode. No data are plotted for $\Lambda^F < \Lambda_D^F$ ($=40{\cdot}1$). In this neutrally stable range of Λ^F, the response is one of linear oscillatory behaviour with the amplitude of the initially imposed deformation. Instead, the focus here is on the linearly unstable range of Λ^F, wherein A is independent of the initial excitation. The discrete data in Figure 7 also clearly indicate independence from the value of h/L. Curve fitting to these data yields the solid line in the figure which takes the form:

$$\frac{A}{h} = 0{\cdot}128(\Lambda^F - \Lambda_D^F)^{0{\cdot}503}. \tag{19}$$

In dimensional form, this relationship suggests that the maximum amplitude scales on plate material, plate geometry and flow parameters as $1/\sqrt{E^*}, \sqrt{(L^3/h}$ and $\sqrt{\rho(U_\infty^2 - U_D^2)}$. Rearrangement of equation (19) also leads to a divergence instability criterion for nonlinear initial disturbances. Thus, an imposed fundamental mode will experience growth for Λ^F greater than a critical value Λ_c^F, where

$$\Lambda_c^F \approx \Lambda_D^F[1 + 1{\cdot}5(A/h)^2]. \tag{20}$$

The form of this relation agrees with equation (12) in Ellen (1977) when h/L (h/a in Ellen's notation) is small, which is the case both here and for most realistic panels. In equation (20), the numerical coefficient differs from that in Ellen. This is because in the present work wall nonlinear effects are only approximated by induced tension, whereas Ellen solved the von Karman nonlinear plate equation. Nevertheless, the result does again show that the linear divergence-onset parameter is modified by structural nonlinearity at order panel-deflection squared. The present result also indicates that nonlinear flow effects are negligible in the

type of problem for which h/L is very small; the h/L flow-effect correction derived by Ellen is too small to be identified in the present numerical experiments. This has been confirmed by further numerical experiments using a linear flow solution; as seen in Figure 2, this model yields no discernible difference in the value of the peak amplitude from which the Λ_c^F threshold is determined.

In Figure 8, the frequency, ω', of the nonlinear oscillations that follow the growth of a small disturbance is shown to depend on both the stiffness ratio, Λ^F, and geometric parameter h/L; ω' has been nondimensionalized using the time scale in equation (18b). The solid lines have been fitted to the discrete data obtained from different numerical experiments and the following determination of ω' is found:

$$\omega' = 0{\cdot}93(h/L)^{1{\cdot}50}(\Lambda^F - \Lambda_D^F)^{0{\cdot}380}. \tag{21}$$

This result is for an undamped plate; results such as those in Figure 2 suggest that this is the highest value that would be found in a physical experiment. For this case, then, the dimensional oscillation frequency approximately scales on plate material, geometric and flow parameters as $(E^*/\rho_W^5)^{1/10}$, $(h/L^4)^{1/3}$ and $[\rho(U_\infty^2 - U_b^2)]^{2/5}$, respectively. In Figure 8, the departures from the above result at high values of $(\Lambda^F - \Lambda_D^F)$ can be explained by the influence of higher-order modes taking part in the destabilization process during the low-amplitude phase of the cycle. This is readily appreciated by contrasting Figure 6 with Figure 3.

3.2. Spring-backed Plate

The foregoing investigation has shown that for the nonlinear response of an unsupported plate a linear flow solution can be used to evaluate saturation amplitudes and deformation

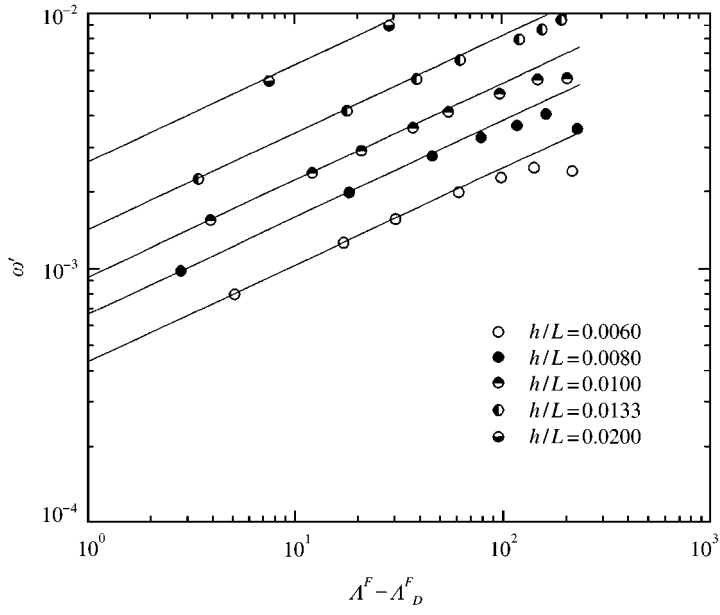

Figure 8. Variation of nondimensional panel oscillation frequency with stiffness ratio, Λ^F for different values of the geometric parameter, h/L. Data for the best-fit lines are generated by equation (21).

forms without undue loss of accuracy. For the simple plate, two length scales, plate thickness, h, and length, L, characterize the problem; the latter because it represents the (half-)wavelength, $\lambda/2$, of the fundamental mode which dominates the stability threshold. Ellen's (1977) analysis shows that nonlinear flow effects enter at order $(w/h)(2h/\lambda)$, whilst structural effects enter at $(w/h)^2$. For realistic unsupported plates, $(2h/\lambda) \ll (w/h)$ and thus the nonlinear effects of the flow are negligible. However, this imbalance does not necessarily hold for a spring-backed plate. Here the critical mode (for linear instability) is determined not by the overall length of the panel but by a combination of wall properties. The wavelength of the critical mode is thus reduced and flow nonlinearity cannot now be neglected.

A suitable characteristic streamwise length is thus sought in order to redefine the nondimensional ratio of destabilizing flow-induced stiffness to wall restorative stiffnesses. This characteristic length must be independent of the panel length, L, since the order of the modes under investigation renders the results applicable to walls of infinite extent. Garrad & Carpenter (1982b) show that disturbances with wavelengths less than that of the seventh mode (on a finite surface) experience negligible influence from the leading and trailling edges. Further, they find that the standing-wave analyses used in studies of finite panels yield critical divergence-onset flow speeds and associated wavelength that agree very closely with those predicted in the travelling-wave analyses of infinite walls. This assumption is also implicit in the modelling of Reynolds & Dowell (1993) for whose flexible wall the eighth is the critical mode. In the present work, a suitable streamwise length scale is therefore based upon the wavelength of the most unstable mode in a linear analysis. In doing this we assume that the nonlinear behaviour originates in the growth of a linearly unstable mode; for this system we have not found any evidence of subcritical instability. For a spring-backed flexible plate, we obtain from Carpenter & Garrad (1986) the following expressions for the onset flow speed and wavelength of divergence instability:

$$U_D = 2\left(\frac{BK^3}{27\rho^4}\right)^{1/8}, \qquad \lambda_D = 2\pi\left(\frac{3B}{K}\right)^{1/4}. \tag{22a,b}$$

Using $\lambda_D/2$ to replace L in equation (17), the stiffness ratio then takes the following modified form:

$$\Lambda^I = \frac{3\pi^3\rho U_\infty^2}{(3BK^3)^{1/4}}. \tag{23}$$

At divergence-onset the critical value of this parameter is given by $\Lambda_D^I = 4\pi^3 (= 124{\cdot}03)$. The present investigations focus on $\Lambda^I > \Lambda_D^I$, since below the critical value linear disturbances lead to attenuated travelling waves when some wall damping is incorporated. A further parameter serves to characterize the non-linear wall behaviour. Analogous to the geometric parameter, h/L, used in Section 3.1 is a (plate) thickness parameter now taking the form $2h/\lambda_D$, which can alternatively be written as $\pi^{-1}[3hK/E^*]^{1/4}$.

For the series of instantaneous wall profiles presented in Figures 9 and 10, the wall-material properties are identical to those used in the linear numerical simulations of Lucey & Carpenter (1992a) which were chosen to model, at least approximately, a rubber-based compliant coating. The plate thickness parameter, $2h/\lambda_D$, therefore takes the numerical value 0·345. This implies high values of plate curvature which should be accounted for by an improved nonlinear wall model incorporating higher-order plate-bending terms. However, in this section, we focus mainly on qualitative features of the results and, in particular, the

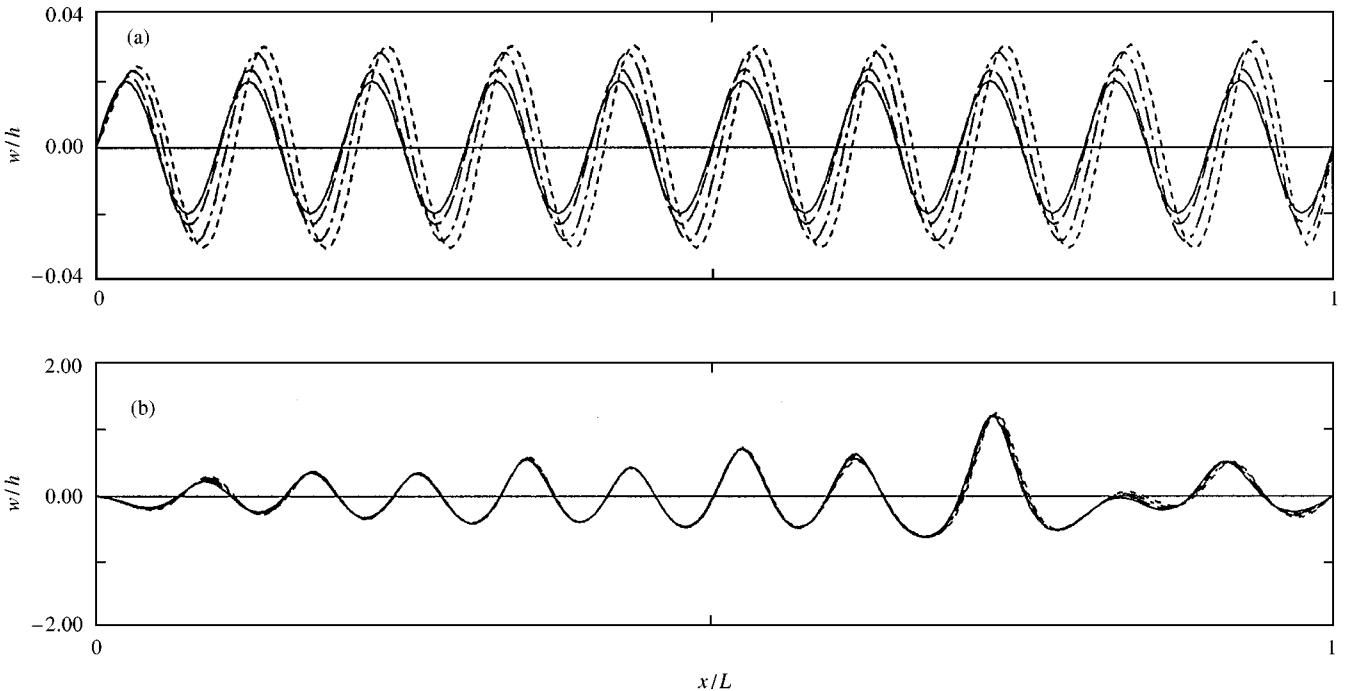

Figure 9. Instantaneous wall profiles at successive times for a highly damped (50%) compliant wall comprising a spring-backed flexible plate. The flow speed (from left to right) is given by $\Lambda^I = 3\pi^3\rho U_\infty^2/(3BK_E^3)^{1/4} = 167{\cdot}8$. The geometric parameter, h/λ_D, is 0·345 and the density ratio, ρ_W/ρ is 0·852. The time between plots in each figure is ΔT and follows the sequence; ——, – –, –·–, - - -. (a) Response at early times: t': $0 \rightarrow 3\Delta T$; (b) nonlinear response at later times: t': $97\Delta T \rightarrow 100\Delta T$.

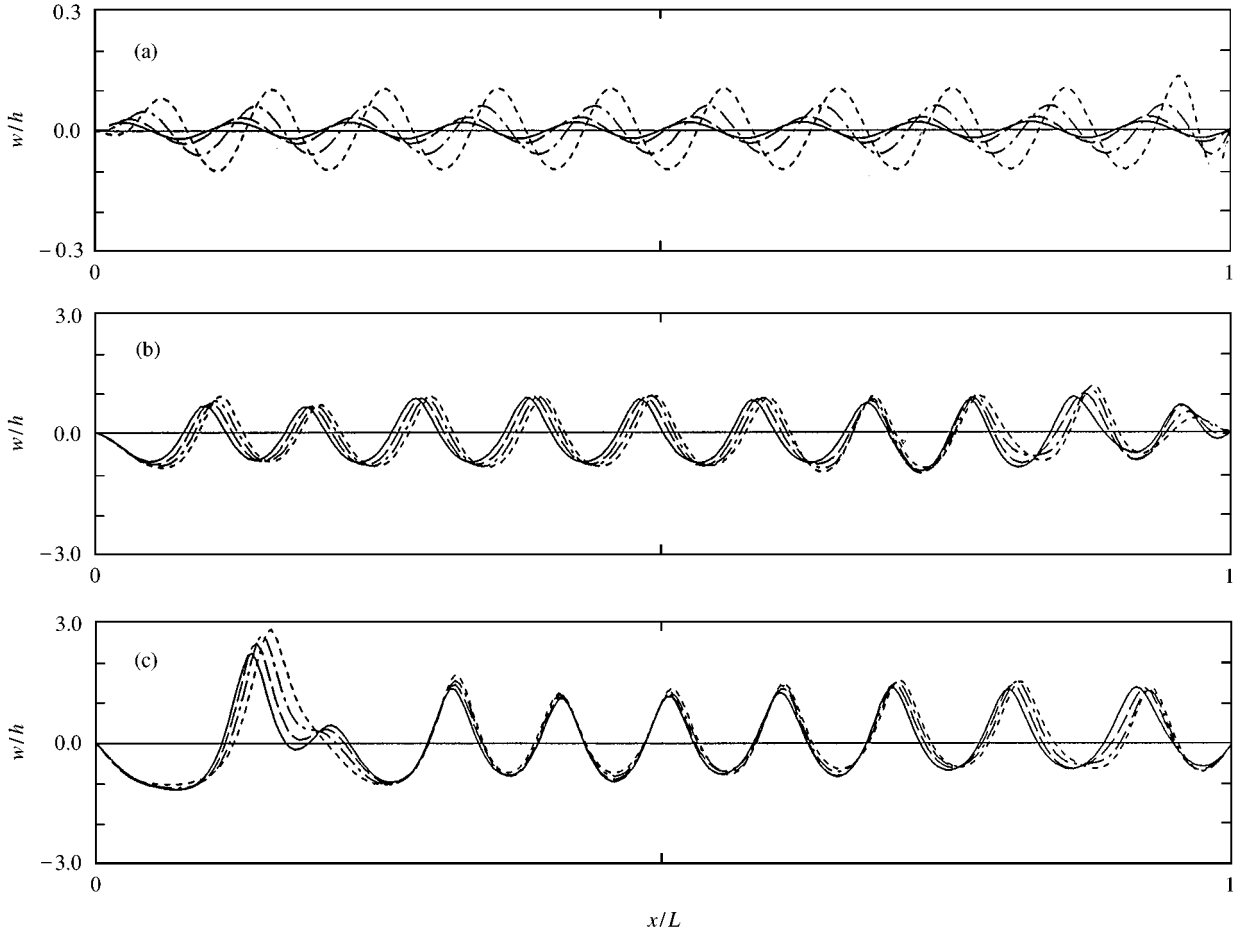

Figure 10. Instantaneous wall profiles at successive times for a highly damped (50%) compliant wall comprising a spring-backed flexible plate. The flow speed (from left to right) is given by $\Lambda^I = 277{\cdot}4$. All other data as in Figure 9. The time between plots in each figure is ΔT and follows the sequence: ——, – –, – · –, - - -. (a) Response at early times: t': $0 \rightarrow 3\Delta T$; (b) transitional response at intermediate times: t': $15\Delta T \rightarrow 18\Delta T$; (c) nonlinear response at later times: t': $25\Delta T \rightarrow 28\Delta T$.

effects of nonlinearity on the flow solution. For detailed quantitative results, compliant-coating dynamics would best be modelled using the finite-element method in a nonlinear extension of Werle *et al.* (1993) which would then be coupled to the present nonlinear flow solution. For the results presented in Figures 9–11, the length of the flexible wall is given by $L = 60h$. However, the results are insensitive to L, provided that it is greater than approximately $4\lambda_D$, (or $23h$ for the present data).

The dynamic behaviour is also dependent on the density ratio ρ_W/ρ, which throughout has been set to 0·852. In Figures 9 and 10 the stiffness ratios are, respectively, 167·8 and 277·4. This data could correspond to a rubber-based compliant coating with flow speeds of 17·5 and 22·5 m/s. A high value of wall damping ($n = 50\%$) has been used in these simulations. In both of these illustrative numerical experiments the initial perturbation takes the form a low-amplitude (of magnitude $h/50$) standing wave of critical wavelength given by equation (22b). This type of linearly unstable mode has been shown by Lucey & Carpenter (1992a) to develop naturally at this stiffness ratio. Here we are only interested in its continued development into the nonlinear regime of response.

Figure 9(a) traces the evolution of surface displacement just after the start of the numerical experiment. Downstream-travelling divergence waves characterize the response. In this and the following figures, the instantaneous wall-profiles have been plotted for successive increments of time†, ΔT. Each ΔT corresponds to 0·41 units of the nondimensional time, t', which is defined by equation (18b), except that for the spring-backed flexible plate λ_D replaces L. Thereafter, continued growth and downstream wave travel ensue, until at much later times the sequence shown in Figure 9(b) suggests that a nearly steady state has been reached. Note that the vertical scale of Figure 9(b) is fifty times that of Figure 9(a). In Figure 9(b) some wave travel still remains; an estimate of the phase speed, c, of this nonlinear divergence wave gives $c/U_\infty \approx 0{\cdot}02$ in contrast with a value of approximately 0·14 in the linear-growth phase of Figure 9(a). The wavelength of the stable nonlinear wave is seen to be only marginally shorter than that of its unstable linear precursor.

At a higher value of Λ^I – equivalently a higher flow speed over the same compliant wall as in Figure 9 – the evolution of the wall deformation is presented in Figure 10. Note that the vertical scale in Figure 10(b, c) is ten times that of Figure 10(a). The disturbance growth rate and phase speed are higher in Figure 10(a) than for the equivalent linear divergence wave of Figure 9(a). Continued downstream travel and amplitude growth – albeit lower than in the linear phase – typifies the intermediate state depicted in Figure 10(b). Finally, the deformation reaches the nearly steady state shown in Figure 10(c). If we use a linear flow solution in the present simulations, the final deformation takes a sinusoidal form and the final nonlinear deformation has a longer wavelength than the linearly unstable divergence wave. These features were predicted by Reynolds & Dowell (1993), who similarly used a linear flow solution and assumed sinusoidal disturbances. Figure 10(c) shows that the use of a nonlinear flow solution yields a nonlinear modal profile that is no longer sinusoidal and which has a similar spatial periodicity to the linearly unstable divergence wave. Other runs with different low-amplitude initial conditions first see an evolution of the deformation into the linearly unstable wave of Figure 10(a) and then the eventual formation of a final state very similar to that seen in Figure 10(c). It is also noted that the nonlinear wave in Figure 10(c) travels slowly in the downstream direction despite the heavy damping. The analyses of

† In generating Figures 9 and 10, each ΔT represents 40 time-steps in the iterative scheme of equations (12a–c). Using a mesh size of $M = 240$, one time-step required approximately six iterations and took 1·26 minutes of CPU time on SUN SPARC Ultra 170E running at 167 MHz.

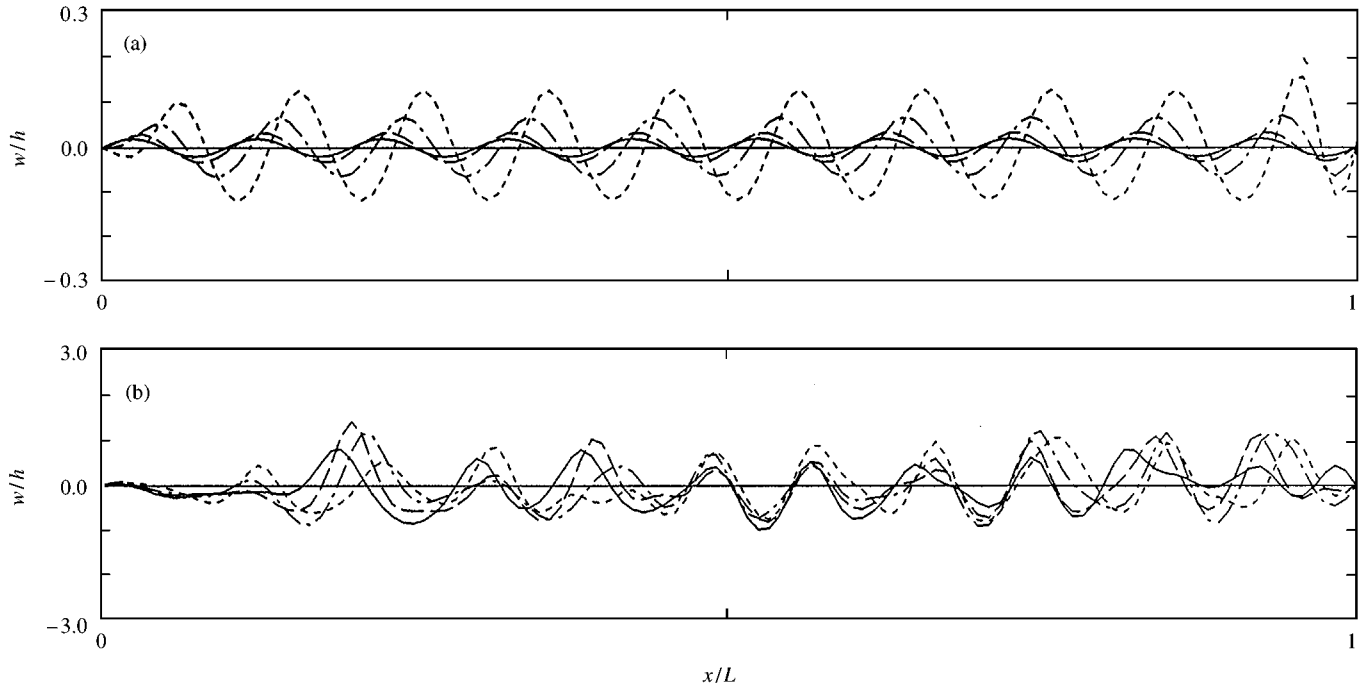

Figure 11. Instantaneous wall profiles at successive times for a lightly damped (5%) compliant wall comprising a spring-backed flexible plate. The flow speed (from left to right) is given by $\Lambda^I = 277{\cdot}4$. All other data as in Figure 9. The time between plots in each figure is ΔT and follows the sequence; ——, – –, – · –, - - -. (a) Response at early times: t': $0 \rightarrow 3\Delta T$; (b) nonlinear response at later times: t': $22\Delta T \rightarrow 25\Delta T$.

Reynolds & Dowell (1993) and Matsuzaki (1981) predict that such damping would ultimately yield a *static* buckled state. The present findings suggest that this prediction was a consequence of using a linear flow solution. As an indicator of averaged wall movement, we have generated (but not presented) time series of wall kinetic energy. After an initial increase due to disturbance growth and wave travel, the kinetic energy then decays but does not asymptote to zero for the case of a nonlinear flow solution; this non-zero kinetic energy is due to the downstream wave travel in the nonlinear response of Figure 10(b, c) when amplitude growth has effectively ceased. In contrast, the equivalent run using a linear flow solution gives a much higher kinetic energy peak, suggesting more rapid disturbance growth than that of Figure 10(a), followed by a steep decay to zero kinetic energy associated with a static state. Finally, at this flow speed, estimates of the nonlinear relative wave phase speed give $c/U_\infty = 0{\cdot}06$, in contrast with a value of 0·25 for the amplifying linear divergence wave seen in Figure 10(a).

Before moving on to a comparison of the present results with experimental evidence, we briefly compare the early stages of the numerical experiments with the predictions of linear theory. In the linear regime of response, the growth rate can be characterized by the imaginary part of a complex angular frequency, ω_I'. From the data which gave Figures 9(a) and 10(a), we estimate ω_I' to take, respectively, the values 0·44 and 1·36. In contrast, standing-wave analysis predicts these to be 1·447 and 2·714, respectively, whilst travelling-wave analysis predicts values of 0·0911 and 0·894. Appropriately, the values generated by the present numerical experiments fall between those predicted by standing-wave and travelling-wave theories. Neither of the theoretical approaches properly models the system studied; standing-wave analysis predicts a static divergence instability with consequent rapid growth, whilst travelling-wave analysis is strictly only applicable to an infinitely long flexible panel with no imposed restraints – here, fixed leading and trailing edges – to wave travel.

The character of the nonlinear wave which evolves in Figure 10 has similarities with the divergence wave experimentally investigated by Gad-el-Hak *et al.* (1984). Although they used a different type of compliant wall, Gad-el-Hak *et al.* described the wave profile as having 'sharp peaks separated by wide valleys' and measured typical relative phase speeds to lie in the range $c/U_\infty : 0 \rightarrow 0{\cdot}05$. The nonlinear wave simulated here show a much better qualitative match both in profile and phase speeds than divergence predictions based on linear theory. In both the present work and the experimental work of Gad-el-Hak *et al.* (1984) and Gad-el-Hak (1986), the rôle of wall damping is found to be important. The evolution of the nearly steady states seen in Figures 9(b) and 10(c) only occur when substantial levels of wall damping are present. Presented in Figure 11 are results of a simulation with all parameters identical to those of Figure 10 but with the damping set to 5% instead of 50%. The growth of unstable linear divergence waves seen in Figure 11(a) is almost identical to the result of Figure 10(a). However, careful comparison shows that the reduction of damping has produced a slight increase in growth rate. Thus, in this stage of response, wall damping behaves in its conventional rôle of wave attenuation. At later times, a typical fully developed response is that seen in Figure 11(b). The characteristic nonlinear divergence waves of Figure 10(c) are not able to form; instead the response is a complex superposition of nonlinear flutter-type waves with high kinetic energy and which appear to persist indefinitely. In the absence of wall damping, aperiodic behaviour was also predicted by Reynolds & Dowell (1993). Also, the experiments of Dugundji *et al.* (1963) using a lightly damped spring-backed flexible plate featured fluttering motions at post–divergence-onset flow speeds rather than slow nonlinear divergence waves. Gad-el-Hak *et al.* (1984) found

their divergence waves on heavily damped viscoelastic compliant walls. Moreover, Gad-el-Hak's (1986) experiments using an elastic wall with little damping features a flutter-type instability instead of divergence waves. The present work suggests that although wall damping is not an essential component of the mechanism causing the *growth* of linear disturbances in divergence instability, its presence is essential if large-amplitude saturated divergence waves are to develop in the nonlinear regime of response.

We have noted that the characteristic waveform of the nonlinear divergence waves seen, for example, in Figure 10(c) qualitatively agrees with the waveform measured by Gad-el-Hak *et al.* (1984). At first sight, this may seem a surprising result because the simple nonlinear plate/spring wall model used here has very different dynamics from the viscoelastic layer used in the experiments of Gad-el-Hak *et al.* However, it does suggest that the waveform may be attributable to nonlinear flow effects. We have noted that when a linear flow solution is used in the present numerical simulations, the final nonlinear response is one of a static buckled sinusoidal deformation instead of the slowly travelling nonlinear divergence waveform seen in experiments. Again, this suggests that the characteristic waveform is attributable to the pressure field associated with the nonlinear flow solution. Because the nonlinear divergence waves travel very slowly, the dominant pressure term is the hydrodynamic stiffness, i.e. the w-dependent hydrodynamic pressure term in equation (1). Accordingly, in Figure 12, we present the evaluation of this steady pressure $\Delta p(0, 0, w)$ for two different amplitudes of the same sinusoidal wall profile. Also plotted in Figure 12 are the competing sums of compliant-wall stiffness generated by plate flexure, spring stiffness and induced tension in the plate. In Figure 12, these flow and wall pressures have been nondimensionalized using $\rho U_\infty^2 (A/h)$. Figure 12(a) is the situation for a low-amplitude ($A/h = 0{\cdot}02$) wall deformation having the same parameters as those used in Figure 10(a) at the start of a dynamic simulation. It is evident that the hydrodynamic stiffness exceeds the wall stiffness and hence the waveform is unstable at this small disturbance amplitude. Figure 12(b) is generated using identical parameters, except that now we have $A/h = 1{\cdot}5$; this is the approximate amplitude of the nonlinear deformations which have evolved in Figure 10(c). However, the wall waveform in Figure 12(b) is set to be sinusoidal. The competing stiffnesses roughly balance and wave growth would not be expected to occur. Furthermore, the profile of hydrodynamic stiffness generated by this large-amplitude sinusoidal disturbance takes a distinctive non-sinusoidal form which closely reflects the characteristic non-linear divergence waveform that evolves in the dynamic simulations and which is found in the experimental work of Gad-el-Hak *et al.* (1984).

In order to characterize the properties of the nonlinear divergence waves typified by Figures 9(b) and 10(c) we have carried out a number of similar numerical experiments and extracted approximate quantitative data on how amplitude, disturbance wavelength and wave phase speed vary with the nondimensional flow speed (stiffness ratio, Λ^I). These data are presented in Figure 13. Note that in Figure 13(a) the amplitude $2A$ represents the vertical distance between the 'valleys' and the 'peaks' of the nonlinear waveform. Also presented in these figures are corresponding results from numerical experiments using a linear flow solution. The nonlinear results show broad qualitative agreement with the experimental measurements of Gad-el-Hak *et al.* (1984) in that divergence-wave amplitudes and phase speeds increase with flow speed, whereas wavelength is relatively unaffected. The linear results show qualitative agreement with the predictions of Reynolds & Dowell (1993) in that both the amplitude and wavelength of the final static state are increased by a rise in flow speed. The contrast between nonlinear and linear flow results clearly demonstrates that nonlinear effects due to the fluid flow cannot be neglected for compliant panels.

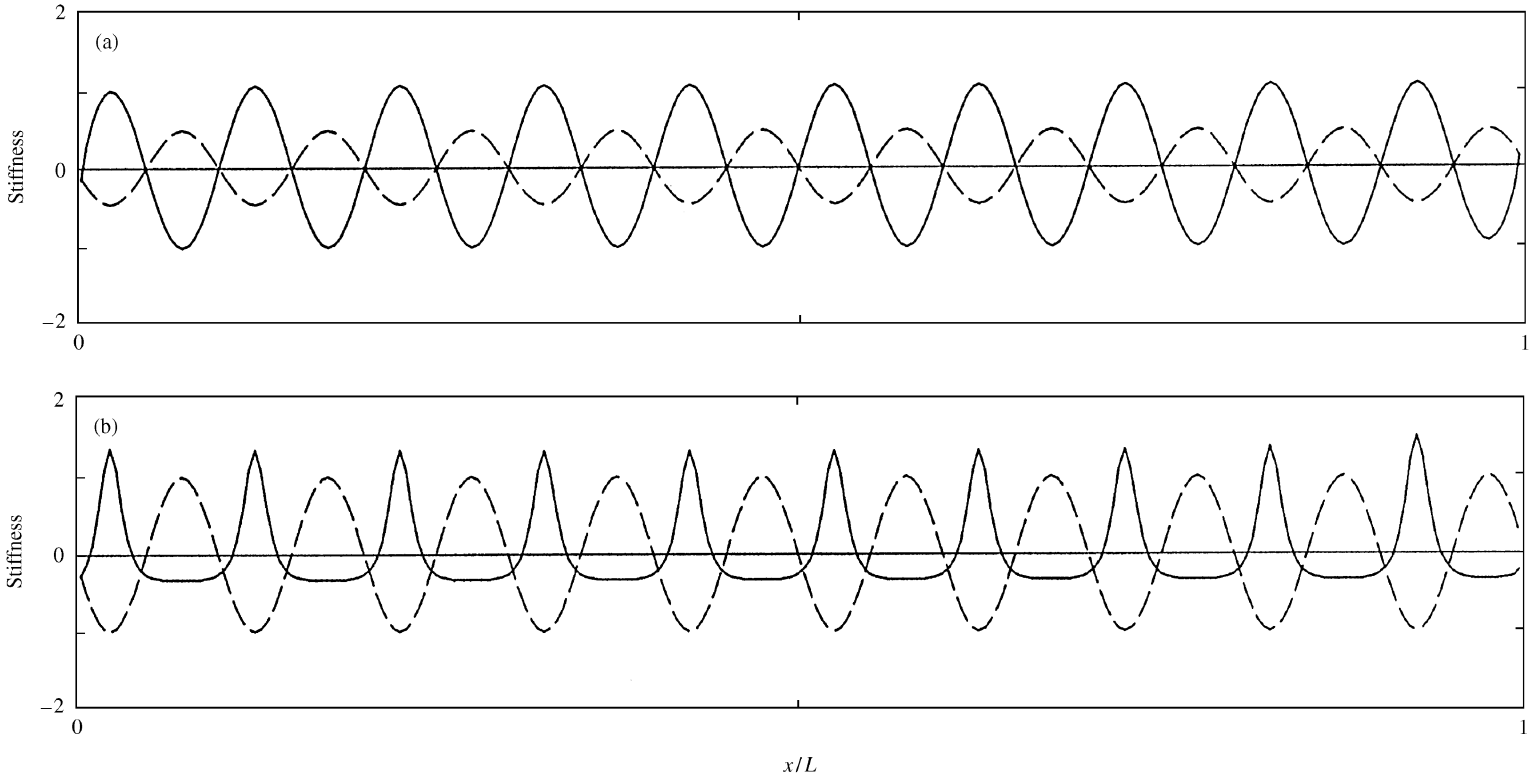

Figure 12. Profiles of non-dimensional hydrodynamic stiffness (——) and flexible-wall restorative stiffness (– –) generated by a static sinusoidal deformation. (a) Low-amplitude wall deformation; (b) high-amplitude wall deformation.

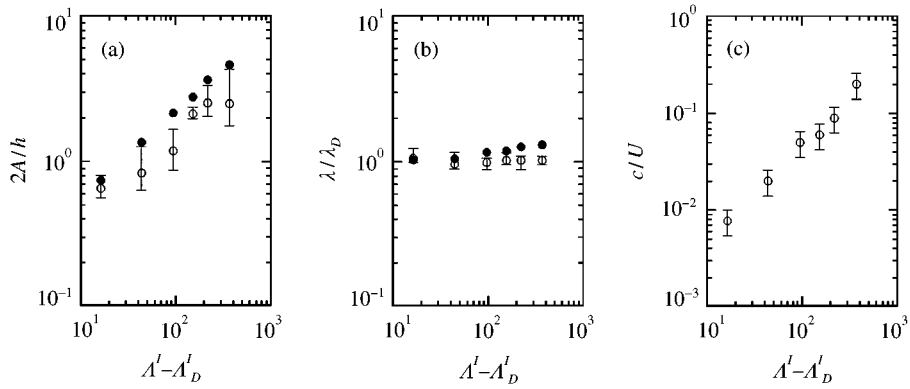

Figure 13. Dependence on flow speed of the properties of nonlinear divergence waves: (a) nondimensional amplitude; (b) spatial periodicity; (c) relative phase speed. Open symbols (○) from nonlinear flow solution; filled symbols (●) from linear flow solution. (Note that the phase speed is always zero for the case of a linear flow solution.)

In closing this section we draw attention to the limitations of the present theoretical and computational model. It is noted that in Figure 10(c) a larger-amplitude peak (with larger wavelength) has developed near the leading edge of the compliant panel. This also appears in numerical experiments at other flow speeds. When extracting the data presented in Figure 13, we have based measurements not on this peak but on the nonlinear divergence waves that occupy the majority of the panel. At present we are uncertain as to whether the leading-edge peak is an artifice of the computational model. If the numerical experiment represented by Figure 10 is continued to times much later than those presented in Figure 10(c), the leading-edge peak experiences continuous growth which modifies the flow field so that the saturated nonlinear waves downstream of it decay in amplitude. In tandem with this effect, one of the most distant downstream peaks becomes amplified in a similar manner to that of the leading-edge peak and the resulting situation is one of a pair of very high-amplitude solitary waves which travel slowly in the downstream direction. This result is not presented because it is felt that the present model is unable to yield an accurate truly final equilibrium state. Investigations have been conducted in order to identify the cause of this behaviour. These include the substitution of 'built-in' leading and trailing edges for the hinged conditions known, in theoretical work [for example Garrad & Carpenter (1982a)], to produce weak logarithmic singularities; we have also used a computational model which properly accounts for the rigid surround. Neither of these modifications significantly change the results of Figure 10(c). Time-step refinement has little effect, and refinement of the mesh postpones, but does not remove, the suspect growth. We therefore believe that the sustained growth of the leading-edge peak may be attributable to numerical divergence. Figure 12(b) has shown that the nonlinear pressure field produces sharp peaks even for a sinusoidal deformation. This tends to produce very local amplification near the peak of the questioned leading-edge disturbance, which in turn sharpens the pressure field, leading to a progressive mechanism for continued amplification of the local peak. Mesh refinement better resolves the flow near the peak and so postpones the numerical divergence; however, it cannot remove the slope discontinuity in the pressure field at the peak. In contrast, the

restorative wall forces plotted in Figure 12(b) are smooth and thus unable to balance the corresponding pressure peak. In reality the strong transverse 'creasing' of the compliant wall at the peak of the continuously growing leading-edge disturbance would introduce wall-structure effects that cannot be represented by the present simple wall model. These further localized, nonlinear wall effects could be expected to balance the sharp peaks in the pressure field. Furthermore, the present work neglects viscous effects in the flow. If these were modelled, then a smoothing of the localized sharp peaks in the pressure field could be expected. A combination of improved wall and flow models would thus yield a computational model better able to arrive at the long-time equilibrium state observed in experiments. Nevertheless, the present study remains useful in that the main features of nonlinear divergence waves are reproduced, despite the use of a simple wall model. These features can therefore be attributed to nonlinear unsteady potential-flow effects that would only be modified by a more complete model.

4. CONCLUSIONS

A computational model, combining boundary-element and finite-difference methods has been developed in order to study the evolution of disturbances of finite flexible panels subjected to a uniform flow. The model allows for nonlinear disturbances in both the flow and wall mechanics. A series of numerical experiments has been conducted for the two cases of an unsupported flexible plate in a flat rigid surround and a spring-backed flexible plate for which the hydroelastic behaviour is largely independent of the panel length. The second case yields results which are applicable to a compliant coating on a flat plate. The investigations have focused on the range of flow speeds for which linear disturbances of the flexible wall would be hydroelastically unstable. In contrast to previous theoretical studies, the present approach does not require any *a priori* specification of the disturbance form, nor is it based upon linearization of perturbations about a known nonlinear buckled state.

The nonlinear response of an unsupported flexible plate is dominated by the fundamental sinusoidal mode. This finding agrees with the predictions of previous analytical studies which evaluate the long-time limit of the panel response. However, we show that a form of wave travel does occur and that this effect is more pronounced at higher flow speeds. A typical flexible panel represented by this study would, in a real application, have a low value of structural damping. It is shown that, although the effect of damping would ultimately yield a static buckled state, nonlinear oscillations would persist for many cycles; we have characterized this oscillatory behaviour through simple formulae. It is also shown that the use of a linear flow solution is sufficient to determine accurately the maximum amplitudes of a nonlinear deformation which develops from the growth of a small disturbance. However, the use of a linear flow solution gives inaccurate results for nonlinear oscillatory behaviour of the panel.

For the case of a spring-backed flexible plate, the critical wavelength of linearly unstable disturbances may be small compared to the panel length. The present simulations have followed the growth of such a disturbance and shown that flow nonlinearity cannot be neglected for this type of flexible boundary. The rôle of wall damping has also been clarified. For a compliant wall with a high value of damping it is shown that unstable small disturbances grow into saturated divergence waves which have markedly different profiles and phase speeds from the initial unstable linear waves. Although the presence of damping is essential for the formation of the nonlinear divergence waves, damping exercises a conventional effect – that of wall-wave attenuation – on the linearly unstable wave. Some

characterization of the nonlinear divergence waves has been carried out. In all respects, the present simulations show good agreement with the divergence waves observed in experiments. We have also been able to show that the characteristics of the divergence waves owe their origin to the hydrodynamic stiffness generated by the flow rather than the nonlinear properties of the wall mechanics. Only limited results have been presented for the case of a compliant panel with a low level of wall damping. In contrast to heavily damped panels, it is shown that the nonlinear response is dominated by a complex superposition of fast flutter-type waves which have sinusoidal profiles. Such responses would be strongly influenced by repeated reflections at the panels ends. Further detailed work needs to be carried out if these are to be understood properly.

Finally, we re-emphasize two limitations of the present work which warrant future research. Firstly, viscous effects have not been incorporated in the present flow model. The principal effect of the boundary layer, present in a physical experiment, would be to scale down the equivalent perturbation pressure based on potential flow calculations. This effect would be significant for disturbances with relatively small ratios of wavelength to boundary-layer thickness, such as those studied in Section 3.2. The recent numerical work of Lucey *et al.* (1997) which simulates boundary-layer flow over an arbitrarily deforming compliant surface confirms this; it also finds that divergence instability is unlikely to occur under a laminar boundary layer. The experiments of Gad-el-Hak *et al.* (1984) clearly demonstrated the difference between laminar and turbulent boundary-layer effects. In their Figure 10, divergence *only* appeared within a turbulent wedge (generated by a roughness element) in an otherwise laminar flow over a flexible panel. Thus, it seems that the divergence instability of the compliant coatings investigated in this paper would only be a feature of turbulent boundary-layer flows. Secondly, very simple nonlinear wall models have been used in this paper. These were chosen to facilitate validation and interpretation of numerical results. The use of a plate-spring model with induced tension has, however, been shown to be deficient for some of the wall profiles that evolve from unstable small disturbances. Thus, improved nonlinear wall models need to be employed if reliable quantitative data are to be extracted from numerical simulations relevant to compliant coatings. The dynamics of such models could readily be coupled with the nonlinear flow solution developed in the present paper.

References

Balasubramanian, R. & Orszag, S. A. 1983 Numerical studies of laminar and turbulent drag reductions. NASA Contract Report No. 3669.

Benjamin, T. B. 1963 The threefold classification of unstable disturbances in flexible surfaces bounding inviscid flows. *Journal of Fluid Mechanics* **16,** 436–450.

Carpenter, P. W. 1990 Status of transition delay using compliant walls. In *Viscous Drag Reduction in Boundary Layers* (eds D.M. Bushnell & J.M. Hefner), pp. 79–113 New York: AIAA.

Carpenter, P. W. & Garrad, A. D. 1986 The hydrodynamic stability of flows over Kramer-type compliant surfaces. Part 2. Flow-induced surface instabilities. *Journal of Fluid Mechanics* **170,** 199–232.

Crighton, D. G. 1989 The 1988 Rayleigh medal lecture: fluid-loading – the interaction between sound and vibration. *Journal of Sound and Vibration* **133,** 1–27.

Davies, C. & Carpenter, P. W. 1997 Numerical simulation of the evolution of Tollmien-Schlichting waves over finite compliant panels. *Journal of Fluid Mechanics* **335,** 361–392.

Dowell, E. H. 1975 *Aeroelasticity of Plates and Shells.* Leyden: Noordhoff.

Dugundji, J., Dowell, E. & Perkin, B. 1963 Subsonic flutter of panels on a continuous elastic foundation. *AIAA Journal* **1,** 1146–1154.

Duncan, J. H., Waxman, A. M. & Tulin, M. P. 1985 The dynamics of waves at the interface between a viscoelastic coating and a fluid flow. *Journal of Fluid Mechanics* **158,** 177–197.

Ellen, C. H. 1973 The stability of simply supported rectangular surfaces in uniform subsonic flow. *Journal of Applied Mechanics* **40,** 68–72.

Ellen, C. H. 1977 The non-linear stability of panels in incompressible flow. *Journal of Sound and Vibration* **54,** 117–121.

Gad-El-Hak, M. 1986 The response of elastic and viscoelastic surface to a turbulent boundary layer. *Journal of Applied Mechanics* **53,** 206–212.

Gad-El-Hak, M., Blackwelder, R. F. & Riley, J. F. 1984 On the interaction of compliant coatings with boundary-layer flows. *Journal of Fluid Mechanics* **140,** 257–280.

Garrad, A. D. & Carpenter, P. W. 1982a On the aerodynamic forces involved in aeroelastic instability of two-dimensional panels in uniform incompressible flow. *Journal of Sound and Vibration* **80,** 437–439.

Garrad, A. D. & Carpenter, P. W. 1982b. A theoretical investigation of flow-induced instabilities in compliant coatings. *Journal of Sound and Vibration* **84,** 483–500.

Gislason, T. 1971. Experimental investigation of panel divergence at subsonic speeds. *AIAA Journal* **9,** 2252–2258.

Hess, J. L. 1973 Higher order numerical solution of the integral equation for the two-dimensional Neumann problem. *Computer Methods in Applied Mechanics and Engineering* **2,** 1–15.

Hess, J. L & Smith, A. M. O. 1966 Calculation of potential flow about arbitrary bodies. *Progress in Aeronautical Science* **8,** 1–138.

Holmes, P. J. 1978 Pipes supported at both ends cannot flutter. *Journal of Applied Mechanics* **45,** 619–622.

Ishii, T. 1965 Aeroelastic instabilities of simply supported panels in subsonic flow. Paper AIAA-65–752.

Kendall, J. M. 1970 The turbulent boundary layer over a wall with progressive waves. *Journal of Fluid Mechanics* **41,** 259–281.

Kornecki, A. 1978 Aeroelastic instabilities of infinitely long plates, I. *Solid Mechanics Archives* **3,** 281–440.

Lucey, A. D. & Carpenter, P. W. 1992a A numerical simulation of the interaction of a compliant wall and inviscid flow. *Journal of Fluid Mechanics* **234,** 121–146.

Lucey, A. D. & Carpenter, P. W. 1992b A study of the hydroelastic stability of a compliant panel using numerical methods. *International Journal of Numerical Methods for Heat and Fluid Flow* **2,** 537–553.

Lucey, A. D. & Carpenter, P. W. 1993a On the difference between the hydroelastic instability of infinite and very long compliant panels. *Journal of Sound Vibration* **163,** 176–181.

Lucey, A. D. & Carpenter, P. W. 1993b The hydroelastic stability of three-dimensional disturbances of a finite compliant panel. *Journal of Sound Vibration* **163,** 527–552.

Lucey, A. D., Cafolla, G. J. & Carpenter, P.W. 1997 Numerical simulation of a boundary-layer flow interacting with a compliant boundary. *Lecture Notes in Physics* **490,** 406–411.

Matsuzaki, Y. 1981 Reexamination of stability of a two-dimensional finite panel exposed to an incompressible flow. *Journal of Applied Mechanics* **48,** 472–478.

Matsuzaki, Y. 1986 Stability of flat plates and cylindrical shells exposed to flows. In *Encyclopedia of Fluid Mechanics*, pp. 476–509. Texas: Gulf Publishing Co.

Matsuzaki, Y. & Ueda, 1980 Reexamination of unsteady fluid dynamic forces on a two-dimensional finite plate at small Mach numbers. *Journal of Applied Mechanics* **47,** 720–724.

Reynolds, R. R. & Dowell, E. H. 1993 Nonlinear aeroelastic response of panels. In *Collection of Technical Papers – AIAA/ASME Structures, Structural Dynamics and Materials Conference*, Part 5, pp. 2566–2576.

Riley, J. R., Gad-El-Hak, M., & Metcalfe, R. W. 1988 Compliant coatings. *Annual Review of Fluid Mechanics* **20,** 393–420.

Weaver, D. S. & Unny, T. S. 1971 The hydroelastic stability of a flat plate. *Journal of Applied Mechanics* **37,** 823–827.

Werle, J., Lucey, A. D. & Carpenter, P. W. 1993 Hydroelastic instability of complex compliant-wall structures in fluid flow. In *Numerical Methods in Laminar and Turbulent Flow* (ed. C. Taylor), Vol. 7, Pt. 2, pp. 1435–1446. Swansea, U.K.: Pineridge Press.

APPENDIX

The matrices of influence coefficients used in equation (6) are generated as follows. Evaluation is carried out at the control point of the ith panel, (X_{C_i}, X_{C_i}), where the sources are distributed over the mth panel which has control point (X_{C_m}, Y_{C_m}). Panel slopes are respectively given by angles α_i and α_m to the horizontal and the source panel has length c_m. Routine integration gives the following expressions for the case $i \neq m$:

$$N_{im} = \frac{a_s}{4\pi} \ln \frac{c_m^2 - 4ec_m + 4f}{c_m^2 + 4ec_m + 4f} + \frac{a_c}{2\pi} \left(\tan^{-1} \frac{2e + c_m}{2b} - \tan^{-1} \frac{2e - c_m}{2b} \right), \tag{A1}$$

$$\Phi_{im} = -\frac{e}{4\pi} \ln \frac{c_m^2 - 4ec_m + 4f}{c_m^2 + 4ec_m + 4f} + \frac{c_m}{8\pi} \ln \frac{(c_m^2 - 4ec_m + 4f)(c_m^2 + 4ec_m + 4f)}{16L^4}$$

$$- \frac{c_m}{2\pi} + \frac{b}{2\pi} \left(\tan^{-1} \frac{2e + c_m}{2b} - \tan^{-1} \frac{2e - c_m}{2b} \right), \tag{A2}$$

$$T_{im}^{\sigma} = -\frac{a_c}{4\pi} \ln \frac{c_m^2 - 4ec_m + 4f}{c_m^2 + 4ec_m + 4f} + \frac{a_s}{2\pi} \left(\tan^{-1} \frac{2e + c_m}{2b} - \tan^{-1} \frac{2e - c_m}{2b} \right), \tag{A3}$$

$$T_{im}^{\lambda} = -\frac{a_c c_m}{2\pi} + \frac{(a_s b - a_c e)}{4\pi} \ln \frac{c_m^2 - 4ec_m + 4f}{c_m^2 + 4ec_m + 4f}$$

$$+ \frac{(a_c b + a_s e)}{2\pi} \left(\tan^{-1} \frac{2e + c_m}{2b} - \tan^{-1} \frac{2e - c_m}{2b} \right), \tag{A4}$$

where

$$a_s = \sin(\alpha_i - \alpha_m), \qquad a_c = \cos(\alpha_i - \alpha_m),$$
$$b = -(X_{C_i} - X_{C_m}) \sin \alpha_m + (Y_{C_i} - Y_{C_m}) \cos \alpha_m,$$
$$e = (X_{C_i} - X_{C_m}) \cos \alpha_m + (Y_{C_i} - Y_{C_m}) \sin \alpha_m,$$
$$f = (X_{C_i} - X_{C_m})^2 + (Y_{C_i} - Y_{C_m})^2.$$

For the case $i = m$, note that the following expressions apply:

$$N_{ii} = \frac{1}{2}, \qquad \Phi_{ii} = \frac{c_m}{2\pi} \left(\ln \frac{c_m}{2L} - 1 \right), \qquad T_{ii}^{\sigma} = 0, \qquad T_{ii}^{\lambda} = -\frac{c_m}{2\pi}.$$

With linear disturbances assumed and leading-order terms retained, the above influence coefficients approximate to

$$N_{im} = \delta_{im}/2, \tag{A5}$$

$$\Phi_{im} = \frac{1}{4\pi} \left\{ (c_m - 2X^*) \ln \left| \frac{c_m - 2X^*}{2L} \right| + (c_m + 2X^*) \ln \left| \frac{c_m + 2X^*}{2L} \right| - 2c_m \right\}, \tag{A6}$$

$$T_{im}^{\sigma} = -\frac{1}{4\pi} \ln \frac{(c_m - 2X^*)^2}{(c_m + 2X^*)^2}, \tag{A7}$$

$$T_{im}^{\lambda} = -\frac{c_m}{2\pi} - X^* \ln \frac{(c_m - 2X^*)^2}{(c_m + 2X^*)^2}, \tag{A8}$$

where $X^* = X_{C_i} - X_{C_m}$.